Universal Angles-Only Cislunar Orbit Determination Using Sparse Collocation

Casey R. Heidrich and Marcus J. Holzinger
University of Colorado Boulder, Boulder, CO USA

ABSTRACT

Orbit determination in non-Keplerian orbit regimes presents challenges due to the chaotic and unpredictable motion in these systems over large time scales. Typical approaches to cislunar orbit determination leverage numerical shooting to produce trajectories in optimization. These methods often break down for measurement gaps on the order of days or hours. This work presents a novel algorithm for cislunar IOD using direct collocation methods. The new approach provides many benefits, including large region of convergence with poor initial guess, as well as increased stability and performance over long observing time scales. An additional modification is made for periodic orbit determination, in which both the orbit and its natural period are estimated by the algorithm simultaneously. IOD leveraging collocation methods may significantly reduce sensor tasking requirements for orbit determination of newly detected objects in cislunar space.

1. INTRODUCTION

The future of space situational awareness (SSA) necessitates substantial leaps in observing algorithms and technologies as a growing number of spacecraft operators set their sights on cislunar space. A critical capability in SSA is the initial orbit determination (IOD) problem. IOD seeks to reconstruct a target orbit from optical measurements across several measurement arcs. In two-body Keplerian dynamics, IOD is a well-defined problem yielding an initial state for batch processing or sequential estimation. Examples of two-body IOD approaches include classical methods such as Laplace, Gauss, and double-r [7], as well as Gooding's method [13] and association of admissible regions (AR) [9]. In contrast, IOD with multi-body dynamics presents a significant challenge due to the lack of analytical solutions (i.e., fewer constants of motion), as well as the chaotic nature of trajectories over long observing periods. Existing efforts in cislunar IOD have largely relied on predictive shooting algorithms to solve for an initial state at epoch [23, 26]. The circular-restricted three body problem (CR3BP) is known to exhibit chaotic, unpredictable behavior, particular over long time scales [14]. In turn, cislunar IOD methods may often fail for measurements gaps on the order of days or even hours. Further, existing approaches often assume perfect angular rate information, imposing burdensome sensor tasking requirements to produce sequential imaging for measurement tracklet interpolation. The state-of-the-art in cislunar IOD will greatly benefit from the development of advanced algorithms that: 1) have a large region of convergence requiring minimal a priori knowledge of the target orbit, and 2) can converge to an accurate solution over long measurement gaps.

This work presents a novel angles-only IOD approach in multi-body systems using direct collocation. The method works via discretization of the solution space over a set of collocation nodes (or "knots"). Transcription of the system dynamics converts the continuous-time problem into a set of interpolating splines at each node. An objective function is designed to minimize the sum-squared measurement residuals at each epoch inversely weighted by the measurement error covariance. Following transcription, the resulting IOD formulation is a large-scale sparse nonlinear programming problem (NLP). For comparison, the number of unknowns with traditional shooting IOD methods is on the order of 10^0, whereas the number of unknown parameters in collocation may be on the order of 10^2 or greater. However, numerical NLP solvers such as IPOPT [3] and SNOPT [12] are widely available and generally meet or exceed capabilities of numerical shooting methods.

A major benefit of the direct method approach is that little to no initial guess information is required to successfully converge to an accurate solution, even over a large search domain. This feature is particularly beneficial for IOD with no prior ephemeris information of an observed object. Direct collocation is commonplace in trajectory optimization

Approved for public release; distribution is unlimited. Public Affairs release approval AFRL-2023-4013. The views expressed are those of the authors and do not reflect the official guidance or position of the United States Government, the Department of Defense or of the United States Air Force.

settings such as optimal control [20] and interplanetary transfers [21] for its convergence properties. These methods have also been previously studied for fast orbit propagation using Chebyshev polynomials [1], Gauss-Legendre [16] collocation, and implicit Runge-Kutta schemes [4], for example. However, the utility of collocation methods in multi-body orbit determination problems is largely unstudied.

This paper demonstrates the advantages of collocation in comparison to traditional shooting methods for non-Keplerian orbit determination. Results demonstrate convergence to accurate solutions from extremely limited initial guess information for the target orbit (such as initializing the algorithm at one of the Lagrange points). The method is highly flexible, allowing for varying observer geometry using angles-only measurement information. Although the CR3BP dynamics are chosen for study, there are no restrictions that preclude application to more realistic orbits using full ephemeris models. When compared to existing shooting methods, the collocation IOD approach proves highly reliable in reconstructing multi-body orbits. Finally, a modified *periodic* IOD algorithm is implemented, demonstrating the capability to fit optical measurements to naturally repeating orbits in the CR3BP system.

SSA is critical to maintaining operational awareness and safety in cislunar space. As the number of objects in the Earth-Moon system continues to expand, operators will require increasing reliability and capability of SSA algorithms. Robust IOD represents a basic requirement for any cislunar observing architecture, as it enables the association of uncorrelated tracks or identification of previously undetected objects from optical measurements. The collocation IOD algorithm presented in this work is a fundamental departure from traditional approaches, demonstrating significant improvements in both solution accuracy and rate of convergence across long measurement intervals with limited initial guess information.

2. NON-KEPLERIAN ORBIT DETERMINATION

Applications of IOD with non-Keplerian orbit dynamics cannot leverage analytical solutions and constants of motion from two-body orbital mechanics. In turn, predicting states forward (or backward) in time requires approximate numerical integration. This section outlines the general multi-body IOD problem, as well as example limitations of explicit integration solution methods.

2.1 Problem Formulation

To begin, suppose the multi-body IOD objective can be posed in terms of a dynamic mapping between hypothesized and observed states at measurement epochs. The nonlinear system dynamics can be written as

$$\dot{\boldsymbol{x}} = \boldsymbol{f}(\boldsymbol{x}, t) \tag{1}$$

for $t \in [t_0, t_f]$ with system state $\boldsymbol{x} \in \mathbb{R}^n$. Measurements of the system state $\boldsymbol{y} \in \mathbb{R}^m$ are modeled by a nonlinear function

$$\boldsymbol{y}_i = \boldsymbol{h}(\boldsymbol{x}_i, t_i) + \boldsymbol{v}_i \tag{2}$$

where $\boldsymbol{v}_i \sim \mathcal{N}(\boldsymbol{0}, R_i)$ is additive Gaussian white noise with intensity $R_i \in \mathbb{R}^{m\times m}$. Suppose a set of observed vectors $\Lambda = \{\boldsymbol{y}_1, \boldsymbol{y}_2, \ldots, \boldsymbol{y}_{n_{\text{obs}}}\}$ are collected at times $t_0 \leq t_i \leq t_f$. A general IOD objective can be formulated in terms of the following distance metric evaluated at each measurement

$$\min_{\boldsymbol{x}_1,\ldots,\boldsymbol{x}_{n_{\text{obs}}}} \quad J = \sum_{i=1}^{n_{\text{obs}}} (\boldsymbol{y}_i - \boldsymbol{h}(\boldsymbol{x}_i, t_i))^{\mathrm{T}} R_i^{-1} (\boldsymbol{y}_i - \boldsymbol{h}(\boldsymbol{x}_i, t_i)) \tag{3}$$

Equation (3) is a general statement for non-Keplerian IOD minimizing the weighted residuals at each measurement epoch. The problem is a nonlinear weighted least squares objective, in which states must be mapped between epochs subject to the dynamics in Eq. (1). Solving this problem can be challenging without precise knowledge of the orbital state. The following section outlines current approaches using explicit integration methods and admissible regions.

2.2 Solution Using Explicit Integration and Admissible Regions

Prior methods have approached solution of Eq. (3) subject to the dynamics of Eq. (1) using numerical shooting methods. These methods can generally be categorized as *indirect* methods using using explicit numerical integration. The solution procedure attempts propagate a hypothesized state at epoch forward (or backward) in time to evaluate the

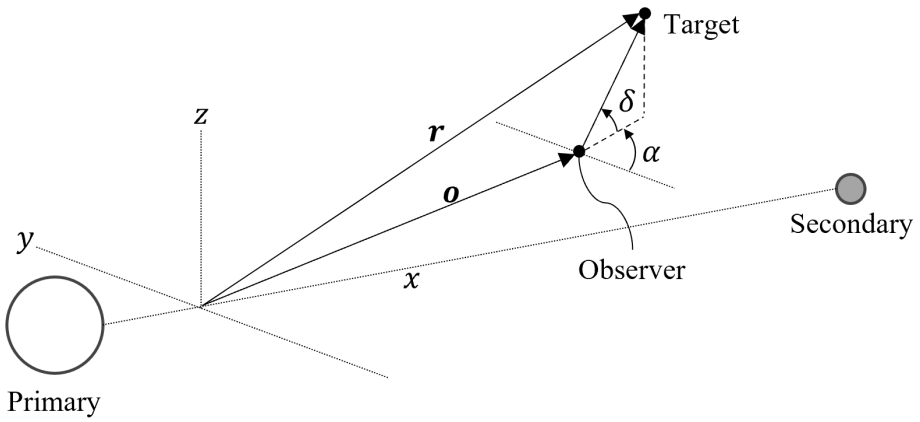

Fig. 1: Illustration of CR3BP coordinate system and RA/DEC angles in synodic frame (not to scale).

IOD objective at every measurement. To outline this approach, first define the *flow function* ϕ as a solution to Eq. (1) with initial state $\boldsymbol{x}_0$

$$\boldsymbol{x}(t) = \phi(t;\boldsymbol{x}_0,t_0), \quad t \in [t_0,t_f] \tag{4}$$

The IOD objective of Eq. (3) can then be rewritten as

$$\min_{\boldsymbol{x}_0} J = \sum_{i=1}^{n_{\text{obs}}} (\boldsymbol{y}_i - \boldsymbol{h}(\phi(t_i;\boldsymbol{x}_0,t_0),t_i))^{\mathrm{T}} R_i^{-1} (\boldsymbol{y}_i - \boldsymbol{h}(\phi(t_i;\boldsymbol{x}_0,t_0),t_i)) \tag{5}$$

in terms of the unknown state at epoch $\boldsymbol{x}_0$. In its stated form, the problem amounts to solving for the position and velocity state at initial epoch that minimizes the measurement residuals at propagated future epochs.

Although the number of unknowns with numerical shooting methods is small ($n = 6$ for 3-DOF motion), multi-body orbit dynamics often exhibit highly nonlinear, chaotic behavior when propagated over long timescales. These methods, while generally stable over short timescales, often break down over large measurement gaps or without a close initial guess. In turn, this makes optimization for the unknown state at epoch challenging.

One approach to overcoming this difficulty utilizes admissible region (AR) information [10, 25]. This approach segments the system states into its undetermined and determined components, $\boldsymbol{x}_u \in \mathbb{R}^{n_u}$ and $\boldsymbol{x}_d \in \mathbb{R}^{n_d}$, respectively, where $n_u + n_d = n$. The undetermined state is then sampled from a bounded AR and a full state at epoch is reconstructed by a mapping from AR components to the full state space. For example, for optical observations with measurement rate information, the given quantities are

$$\boldsymbol{x}_d = [\alpha, \dot{\alpha}, \delta, \dot{\delta}]^{\mathrm{T}} \tag{6}$$

where α and δ are the right ascension (RA) and declination (DEC) angles, respectively. An illustration of these angles is given in Figure 1. At each observation, the hypothesized range ρ and range-rate $\dot{\rho}$ are sampled from the AR at time t_i such that

$$\boldsymbol{x}_u = [\rho, \dot{\rho}]^{\mathrm{T}} \tag{7}$$

A state estimate at t_i can then be reconstructed from following the methodology in Worthy and Holzinger [24]. For angles-only IOD, the angle rates are not assumed, meaning an additional two quantities must be pulled from the AR. Further, for non-Keplerian orbits, AR methodologies are not well-developed and may not provide sufficient information to accurately sample undetermined quantities.

Example IOD results using shooting methods for a simple cislunar observing scenario are shown in Figure 2. These cases were specifically chosen to outline failure modes of explicit integration methods. We note that these methods are able to converge to accurate solutions in many cases [23], particularly over short measurement time scales. However, the reliability of these methods for generalized observing architectures with long observing gaps or complex orbits is not assured. While not exhaustive, the example cases illustrate limitations of these methods in the highly nonlinear CR3BP system. In turn, this places burdensome operational considerations and sensor tasking requirements for orbit determination in the cislunar domain.

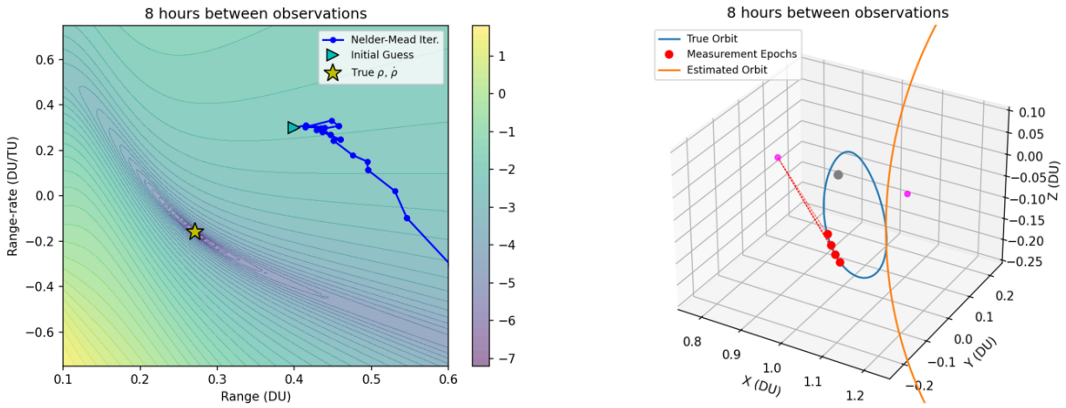

(a) Initial guess error

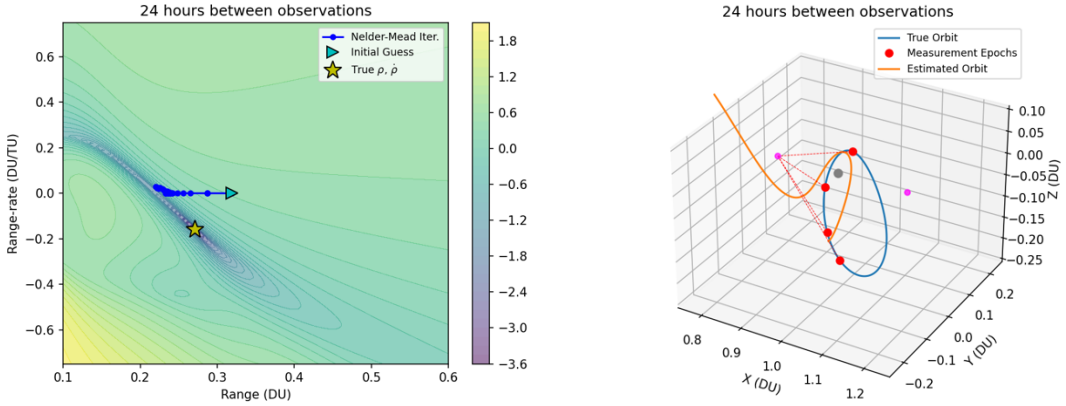

(b) Large measurement interval

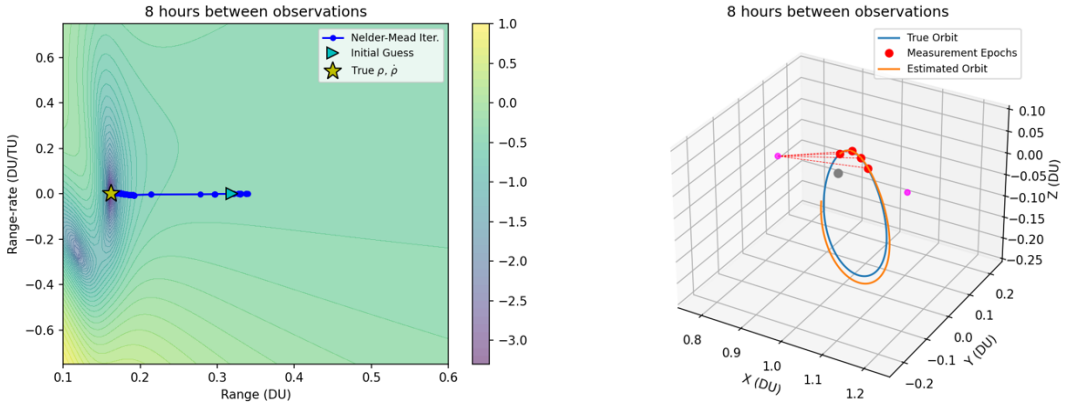

(c) Phasing in target orbit

Fig. 2: Illustration of failed IOD cases using numerical shooting methods (L2 Southern Halo target and L1 observer). In general, without a close initial guess and closely-spaced measurements, these methods tend to break down due to nonlinear, chaotic behavior in the CR3BP dynamics.

3. SOLUTION USING SPARSE COLLOCATION

The objective of this work is to develop a novel collocation IOD algorithm using *direct* methods. In this approach, the solution space is discretized into nodes (or "knots") in time. The state at each node is optimized at each iteration independently to minimize the IOD objective in Eq. (3). Transcription of the dynamics using piecewise interpolating splines enforces Eq. (1) implicitly, ensuring the resulting solution is a feasible trajectory of the system. Direct methods tend to have a wide region of convergence and low sensitivity to initial guess errors. Although these benefits are well-known in trajectory optimization settings [11], direct methods are under-utilized for IOD and nonlinear batch estimation problems in general. Details of the collocation IOD algorithm are given in the following sections, along with examples and case studies of interest relevant to cislunar SSA.

3.1 Transcription to Nonlinear Programming Problem

The primary feature of the direct collocation approach is to discretize the solution space while enforcing governing differential equations through a set of equality constraints. A feasible solution of the discretized problem must then satisfy the system dynamics to the degree of accuracy implied by the transcription scheme. The reader is referred to Refs. [2, 22, 17] for further details.

The transcription process is outlined as follows. The time domain is divided into N discrete times over the mesh defined as

$$t_k = t_1 < t_2 < \cdots < t_N \tag{8}$$

Throughout this paper, the k-th subscript will indicate the index of a collocation node point, whereas the i-th subscript will represent the index of a specified measurement epoch. In general, these times cannot be assumed coincident without tying the mesh spacing to the measurement times. For the purposes of this work we utilize a uniform mesh spacing, although a non-uniform mesh is equally valid.

The states at each node $\boldsymbol{x}_k = \boldsymbol{x}(t_k)$ are concatenated into a parameter vector $\boldsymbol{X} \in \mathbb{R}^{nN}$ defined as

$$\boldsymbol{X}^{\mathrm{T}} = [\boldsymbol{x}_1^{\mathrm{T}}, \boldsymbol{x}_2^{\mathrm{T}}, \ldots, \boldsymbol{x}_N^{\mathrm{T}}] \tag{9}$$

The nN total number of unknowns is a function of both the mesh grid spacing and the state dimension. The IOD objective in Eq. (3) can then be stated as

$$\min_{\boldsymbol{x}_1,\ldots,\boldsymbol{x}_N} J = \sum_{i=1}^{n_{\mathrm{obs}}} (\boldsymbol{y}_i - \boldsymbol{h}(\boldsymbol{x}_i, t_i))^{\mathrm{T}} R_i^{-1} (\boldsymbol{y}_i - \boldsymbol{h}(\boldsymbol{x}_i, t_i)) \tag{10}$$

Note that, since the measurement times t_i are not assumed coincident with the node times t_k, an interpolation of the state $\boldsymbol{x}_i$ at each measurement epoch must be performed with respect to the collocation mesh. This procedure is outlined in the next section.

The differential equation in Eq. (1) is replaced by a set of equality (or "defect") constraints of the form

$$\boldsymbol{g}_k(\boldsymbol{x}_k, \boldsymbol{x}_{k+1}, t_k, t_{k+1}) = \boldsymbol{0}, \quad k = 1, \ldots, N-1 \tag{11}$$

where the constraints $\boldsymbol{g}_k$ depend on the collocation scheme. For example, using trapezoidal collocation [17] gives

$$\boldsymbol{g}_k = \boldsymbol{x}_{k+1} - \boldsymbol{x}_k - \frac{1}{2} h_k (\boldsymbol{f}_{k+1} + \boldsymbol{f}_k) = \boldsymbol{0} \tag{12}$$

where $h_k = t_{k+1} - t_k$. The $\boldsymbol{f}_k = \boldsymbol{f}(\boldsymbol{x}_k, t_k)$ notation indicates the system dynamics evaluated at time t_k. Trapezoidal collocation constraints result from using trapezoidal quadrature to approximate the integral of the dynamics between times t_k and t_{k+1} with a quadratic spline interpolation of the state.

As the accuracy of the quadrature scheme is directly tied to the mesh spacing interval, it is often desirable to use a higher-order approximation of the system dynamics. For example, the Hermite-Simpson collocation method represents the state trajectory using cubic splines, giving the following defect constraint

$$\boldsymbol{g}_k = \boldsymbol{x}_{k+1} - \boldsymbol{x}_k - \frac{1}{6} h_k (\boldsymbol{f}_k + 4\boldsymbol{f}_{k+\frac{1}{2}} + \boldsymbol{f}_{k+1}) = \boldsymbol{0} \tag{13}$$

Note that in contrast to Eq. (12), the defect constraint in Eq. (13) requires an additional evaluation of the system dynamics $\boldsymbol{f}_{k+\frac{1}{2}}$ at the midpoint of the segment $\boldsymbol{x}_{k+\frac{1}{2}}$. This point can be evaluated from an interpolant of the state trajectory at time $t_{k+\frac{1}{2}}$ as follows

$$\boldsymbol{x}_{k+\frac{1}{2}} = \frac{1}{2}(\boldsymbol{x}_k + \boldsymbol{x}_{k+1}) + \frac{1}{8}h_k(\boldsymbol{f}_k - \boldsymbol{f}_{k+1}) \tag{14}$$

Although many choices exist for transcribing the system dynamics (see Betts [2]), for this work we focus on trapezoidal and Hermite-Simpson collocation.

Regardless of the transcription method chosen, the objective in Eq. (10) subject to constraints in Eq. (11) can be written compactly as the

$$\left(P^N\right) \begin{cases} \text{minimize} & J(\boldsymbol{X}) \\ \text{subject to} & \boldsymbol{g}(\boldsymbol{X}) = \boldsymbol{0} \\ & \boldsymbol{X}_L \leq \boldsymbol{X} \leq \boldsymbol{X}_U \end{cases} \tag{15}$$

where $\boldsymbol{X}_L$ and $\boldsymbol{X}_U$ are the lower and upper bounds, respectively, on the unknown parameters $\boldsymbol{X}$. In general, these limits need not be overly restrictive or require significant knowledge of the solution domain. Along-the-path inequality constraints are also feasible, but these are left for future work. The continuous-time IOD problem has been converted to a large scale nonlinear-programming (NLP) problem in Eq. (15). Given an initial guess for the unknowns, a solution can be found with widely available numerical NLP solvers such as SNOPT [12] or IPOPT [3].

3.2 Measurement Interpolation

The IOD objective in Eq. (10) as transcribed to a NLP problem must be evaluated at each measurement epoch. However, the measurement times may not match exactly with constructed grid times. Two approaches are plausible to overcome this problem. The first option is to construct a dense mesh in which measurements can be correlated to a single node. In this case, the objective (and its gradient) are only evaluated at this isolated node for each measurement epoch. However, this approach introduces additional numerical overhead in evaluating the NLP constraints for more unknowns, due to the insertion of synthetic node times coinciding with each measurement. A second, more efficient approach, is to use interpolating splines to determine the solution state between node points. Although this introduces implementation and algorithm complexity, it decouples the node spacing entirely from the measurement epochs. An illustration of these two approaches is given in Figure 3. For periodic IOD covered in the following section, grid interpolation is strictly required.

Although interpolation is a relatively straight-forward task in general, a number of complexities exist when applied in the context of the collocation IOD algorithm, including: 1) the interpolation method is dependent on the transcription scheme itself, 2) the gradient and its objective must be evaluated at the two nearest-neighbor nodes relative to each measurement, and 3) large discontinuities in the measurement model (such as RA angle-wrapping) are not well-approximated by smooth interpolating splines. This section outlines an interpolation approach that accounts for these properties.

First, noting that Eq. (10) must evaluate the state $\boldsymbol{x}_i$ at each predicted measurement, we consider the state at each nearest-neighbor nodes $\boldsymbol{x}_k$ and $\boldsymbol{x}_{k+1}$ such that $t_k \leq t_i \leq t_{k+1}$. We also introduce the following notation $\Delta_i = t_i - t_k$ as the time differential between the first mesh point and measurement. An interpolated state can be constructed generally as

$$\boldsymbol{x}_i = \boldsymbol{c}_0(\boldsymbol{x}_k, \boldsymbol{x}_{k+1}) + \boldsymbol{c}_1(\boldsymbol{x}_k, \boldsymbol{x}_{k+1})\Delta_i + \boldsymbol{c}_2(\boldsymbol{x}_k, \boldsymbol{x}_{k+1})\Delta_i^2 + \ldots \tag{16}$$

where the coefficients $\boldsymbol{c}_0, \boldsymbol{c}_1, \boldsymbol{c}_2, \ldots$ are determined by the transcription scheme. For example the trapezoidal quadrature method approximate the system dynamics linearly in time, resulting in a quadratic spline interpolation of the integrated state

$$\boldsymbol{x}_i = \boldsymbol{x}_k + \boldsymbol{f}_k\Delta_i + \frac{1}{2}\frac{\Delta_i^2}{h_k}(\boldsymbol{f}_{k+1} - \boldsymbol{f}_k) \tag{17}$$

Note that the preceding interpolant is valid only for $t_i \in [t_k, t_{k+1}]$ and is not extrapolated outside of these bounds. Similarly, for higher-order Hermite-Simpson collocation the system dynamics are interpolated quadratically, resulting in a cubic interpolation of the integrated state of the form

$$\boldsymbol{x}_i = \boldsymbol{x}_k + \boldsymbol{f}_k\Delta_i + \frac{1}{2h_k}(-3\boldsymbol{f}_k + 4\boldsymbol{f}_{k+\frac{1}{2}} - \boldsymbol{f}_{k+1})\Delta_i^2 + \frac{1}{3h_k^2}(2\boldsymbol{f}_k - 4\boldsymbol{f}_{k+\frac{1}{2}} + 2\boldsymbol{f}_{k+1})\Delta_i^3 \tag{18}$$

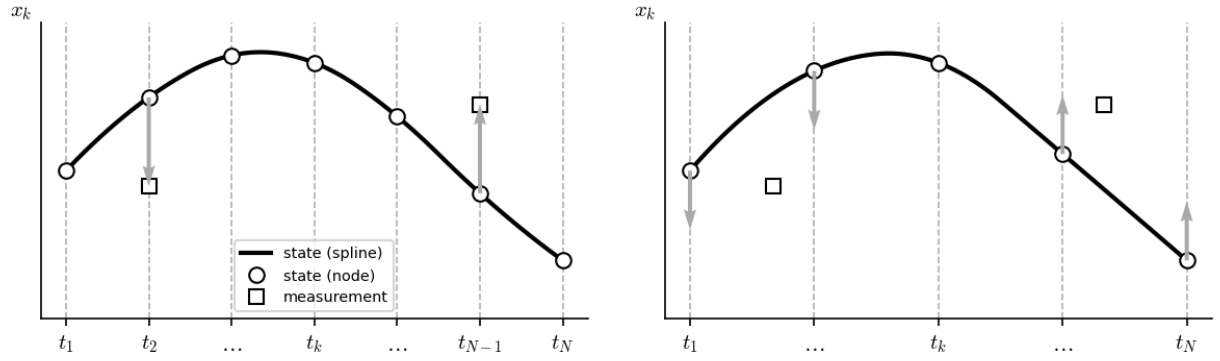

(a) Dense mesh

(b) Sparse mesh

Fig. 3: Heuristic comparison of dense and sparse mesh schemes with interpolating measurement. Arrows represent non-zero gradient evaluations at a given node.

Equations (17) and (18) give the necessary expressions for evaluating the NLP objective at each measurement as a function of the mesh grid. This information must also be reflected in computation of the objective gradient and constraint Jacobian, which is discussed in the following section.

3.3 Gradient and Jacobian Structure

Iterative NLP solvers (such as IPOPT) require an evaluation of the objective gradient and constraint Jacobian with respective to the unknown parameter vector $\boldsymbol{X}$. These expressions are briefly outlined here for context. Let us introduce the notation

$$\nabla_k(\cdot) = \left(\frac{\partial(\cdot)}{\partial \boldsymbol{x}_k}\right) \tag{19}$$

as the gradient of a quantity with respect to the state at a specified node k. Referring to the IOD objective in Eq. (10), the gradient at node k corresponding to measurement i is

$$\nabla_k J = -2(\boldsymbol{y}_i - \boldsymbol{h}(\boldsymbol{x}_i, t_i))^{\mathrm{T}} R_i^{-1} \left(\frac{\partial \boldsymbol{h}_i}{\partial \boldsymbol{x}_i}\right)\left(\frac{\partial \boldsymbol{x}_i}{\partial \boldsymbol{x}_k}\right) \tag{20}$$

Because the interpolating function in Eq. (16) includes both of its nearest-neighbor nodes for each measurement, the gradient must also be evaluated at node $k+1$ as

$$\nabla_{k+1} J = -2(\boldsymbol{y}_i - \boldsymbol{h}(\boldsymbol{x}_i, t_i))^{\mathrm{T}} R_i^{-1} \left(\frac{\partial \boldsymbol{h}_i}{\partial \boldsymbol{x}_i}\right)\left(\frac{\partial \boldsymbol{x}_i}{\partial \boldsymbol{x}_{k+1}}\right) \tag{21}$$

The first Jacobian $(\partial \boldsymbol{h}_i)/(\partial \boldsymbol{x}_i)$ is evaluated based on the form of the measurement model. For angles-only IOD, the measurement function is generally right ascension (RA) and declination (DEC), or the line-of-sight (LOS) vector. Expressions for $(\partial \boldsymbol{x}_i)/(\partial \boldsymbol{x}_k)$ and $(\partial \boldsymbol{x}_i)/(\partial \boldsymbol{x}_{k+1})$ are developed as a function of the interpolation method (and therefore transcription scheme) in the Appendix.

For clarity, it can be shown that the structure of the objective gradient takes the form

$$\left(\frac{\partial J}{\partial \boldsymbol{X}}\right)^{\mathrm{T}} \sim \begin{bmatrix} \mathbf{1}_n^{\mathrm{T}} & \mathbf{1}_n^{\mathrm{T}} & \mathbf{0}_n^{\mathrm{T}} & \cdots & \mathbf{0}_n^{\mathrm{T}} & \mathbf{1}_n^{\mathrm{T}} & \mathbf{1}_n^{\mathrm{T}} & \cdots \end{bmatrix}^{\mathrm{T}} \in \mathbb{R}^{Nn} \tag{22}$$

where $\mathbf{1}$ refers to a vector with all entries equaling one. Note that Eq. (22) is not a strict equality; it serves only to illustrate the zero and non-zero entries of the objective gradient. It is interesting to note that the gradient is evaluated at discrete points in the solution space, which is in contrast to most trajectory optimization problems that attempt to

Case No.	Target Orbit	Initial Guess	Nodes	NLP Iterations	NLP Error	CPU Time
1	L2 S Halo	L2	16	15	1.7850E-6	0.293 s
2	DRO	L2	20	18	3.6442E-6	0.415 s
3	L4 Long Period	L4	45	70	1.91784E-6	3.347 s
4	Northern Dragonfly	L2	40	43	2.1214E-5	1.182 s

Table 1: Summary of example cislunar observing cases using collocation IOD algorithm (L1 N Halo observer).

optimize a terminal or integral cost [22]. Similarly, the structure of the constraint Jacobian can be illustrated as follows

$$\left(\frac{\partial \boldsymbol{g}}{\partial \boldsymbol{X}}\right) \sim \begin{bmatrix} \mathbf{1}_{n\times n} & \mathbf{1}_{n\times n} & \mathbf{0}_{n\times n} & \cdots & \mathbf{0}_{n\times n} \\ \mathbf{0}_{n\times n} & \mathbf{1}_{n\times n} & \mathbf{1}_{n\times n} & \cdots & \mathbf{0}_{n\times n} \\ \vdots & \vdots & \ddots & \ddots & \vdots \\ \mathbf{0}_{n\times n} & \mathbf{0}_{n\times n} & \cdots & \mathbf{1}_{n\times n} & \mathbf{1}_{n\times n} \end{bmatrix} \in \mathbb{R}^{n(N-1)\times nN} \tag{23}$$

where we again emphasize that Eq. (23) is not a strict equality. The individual entries of the constraint Jacobian are found based on the transcription method. These quantities are given in the Appendix.

3.4 Case Studies and Discussion

The preceding sections outline a novel IOD algorithm utilizing direct collocation. In contrast to existing strategies, the approach relies on implicit integration between nodes to ensure a trajectory satisfies the system dynamics. One of the major benefits of this approach is to significantly reduce the sensitivity of the algorithm to errors in the initialization of the algorithm. Whereas shooting methods have leveraged admissible regions (with assumed angles and angle rates information) to generate an initial state at epoch, the collocation IOD algorithm can converge from a wide range of initial guesses. Moreover, results indicate that the method is robust to widely-spaced measurements over long observing time scales. These convergence properties also benefit applications requiring minimal human intervention, such as autonomous catalog maintenance of a large number of tracked objects in cislunar space.

Table 1 summarizes representative example cislunar observing cases. Measurement time scales and cadences vary by case. The algorithm is initialized with an initial guess coinciding with a stationary Lagrange point of the Earth-Moon system. These points are widely known and easy to compute. Application of admissible region methodologies may enable further refinement of an initial guess at epoch; however, the purpose of the following results is to illustrate a wide region of attraction of the collocation IOD algorithm starting from a poor initial guess. The NLP solver was set to a 1E-5 convergence tolerance threshold.

Figure 4 shows reconstructed orbits in 3-D position space. The initial guess for each case corresponds to a Lagrange point of the Earth-Moon system, which can be interpreted as a stationary orbit at this point. Measurement epochs and relative LOS vectors are also shown in red. Note that these correspond to angular quantities at each measurement (RA/DEC), not absolute position measurements. The node points are plotted along with an interpolation between nodes consistent with the transcription scheme. The number of nodes in each case were chosen by inspection, although automated mesh refinement techniques could be applied to produce finer solutions. The CPU time for solution is on the order of seconds, indicating that the algorithm could be implemented for online applications, without relying on extensive ground operations for computing initial orbits.

Further support of these findings is evident from Figure 5, which shows a time history of RA/DEC angles. These angular quantities are computed across the full observing period for visualization, but it is emphasized that measurement information is only utilized in the algorithm at the prescribed epochs (red markers). These results also highlight the range of observing timescales that are possible with the collocation IOD approach. In Cases 1 and 2, the relatively shorter orbit periods allow for IOD on the order of 3-5 days between measurements. The L4 Long Period orbit in Case 3, however, succeeded with a substantial gap between measurements of about 4 weeks. Prior methods using explicit shooting methods would be unlikely to see convergence in these difficult observing scenarios. Further, due to the long timescale of the L4 Long Period family, it is unlikely this orbit could be accurately reconstructed without these widely-spaced measurements.

The convergence rate and accuracy of each IOD case is summarized in Figure 6. The total iterations required for convergence varies based on situational observing geometries and orbits. The L2 S Halo and DRO cases converge

relative quickly in less than 20 iterations, whereas the L4 and Dragonfly orbits take longer due to the complexity of the orbits and the time between measurements. The final objective value depends on the error of the implicit integration implied by the collocation scheme. Finer grids or mesh refinements would improve these accuracies at the cost of greater computing costs. For the purposes of this study, however, the results are sufficiently accurate to fully reconstruct the target orbit from widely-spaced optical observations.

While no AR information is used in the algorithm, AR methodologies could be applied to further reduce the feasible search space of the NLP problem. In addition, there is no strict requirement that an observer be stationed in any particular orbit. For example, Earth-based observers could also be considered, although low observability in angular measurements of near-Lunar orbits as seen by ground observers is a limiting factor.

4. PERIODIC INITIAL ORBIT DETERMINATION

Periodic orbits in the CR3BP system are a topic of high importance in cislunar SSA [8, 15]. These orbits have the special property of repeating natural motion as seen by the rotating synodic frame. This behavior is desirable for observing in the Earth-Moon environment, as stable repeating orbits allow for predictable motion with lower station-keeping maneuver requirements. Cislunar periodic orbit determination has been approached using Gaussian Mixture Model Estimation Filters [5], observability analysis about Libration points [19], or machine learning classification [18], for example. The capability to autonomously estimate a repeating orbit and its period simultaneously from optical measurements remains an ongoing area of research.

In this section, we modify the collocation IOD algorithm for periodic orbit determination in non-Keplerian systems. The process maintains the benefits of the direct collocation scheme, requiring minimal a priori knowledge to initialize the algorithm. The method also does not rely on sourcing pre-computed periodic orbit tables. The approach is outlined in the following sections.

4.1 Time Normalization

Repeating natural motion of a dynamic system in general can be stated as a *periodicity* constraint of the form

$$\boldsymbol{x}(t+T) = \boldsymbol{x}(t) \tag{24}$$

where T is the period of the orbit. In the preceding sections, the time scale was fixed as the delta between the initial and final observation epochs. For periodic IOD, the total time scale is a function of the unknown variable T. It is therefore helpful to normalize the problem over a new time interval $\tau \in [-1,1]$. Note that the original time variable $t \in [t_0, t_f]$ can be recovered by an affine transformation [11] with no loss of generality

$$t = \frac{t_f - t_0}{2}\tau + \frac{t_f + t_0}{2} \tag{25}$$

For notational convenience, we restrict our application to the case where $t_0 = 0$ and $t_f = T$ without loss of generality. Applying Eq. (25) over the the mesh times t_k and measurement epochs t_i gives the relations

$$t_k = \frac{T}{2}\tau_k + \frac{T}{2}, \quad t_i = \frac{T}{2}\tau_i + \frac{T}{2} \tag{26}$$

The system dynamics Eq. (1) must also be transformed to the new time variable as

$$\frac{\mathrm{d}\boldsymbol{x}}{\mathrm{d}\tau} = \boldsymbol{f}(\boldsymbol{x}(\tau), \tau) \tag{27}$$

The periodicity constraint in Eq. (24) can then be stated as simply

$$\boldsymbol{x}(-1) - \boldsymbol{x}(1) = \boldsymbol{0} \tag{28}$$

where the period T has been absorbed into the affine transformation in Eq. (25).

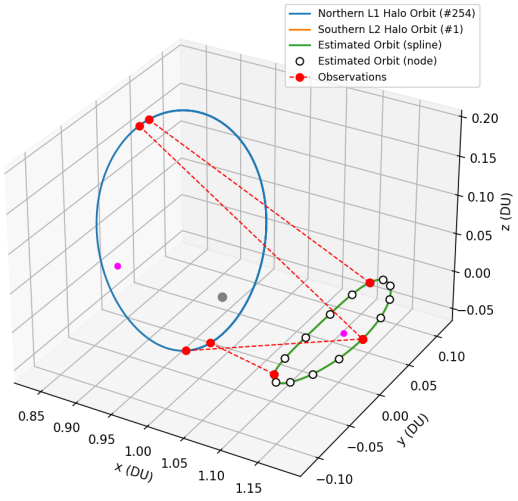

(a) Case 1 (L2 S Halo)

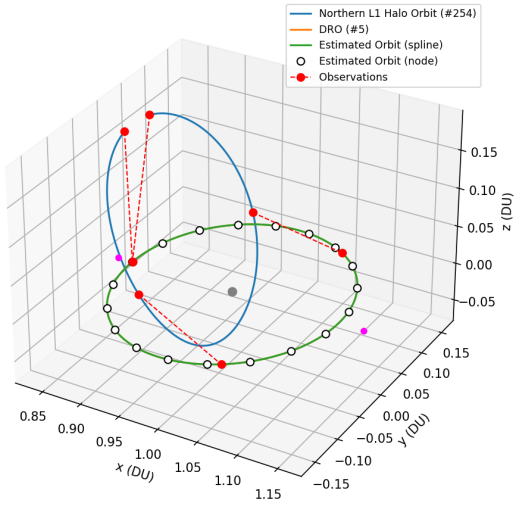

(b) Case 2 (DRO)

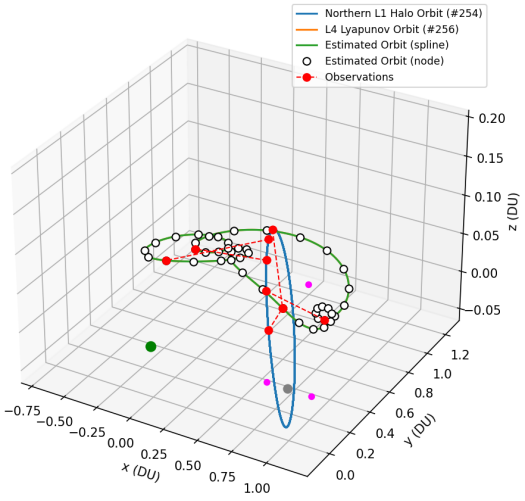

(c) Case 3 (L4 Long Period)

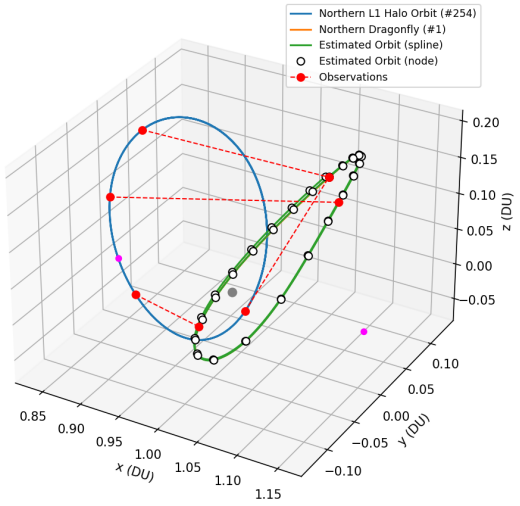

(d) Case 4 (Northern Dragonfly)

Fig. 4: 3-D visualization of observer and reconstructed target orbits using collocation IOD algorithm.

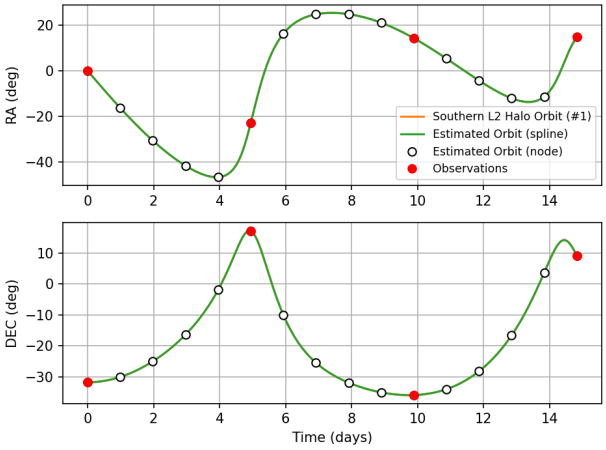

(a) Case 1 (L2 S Halo)

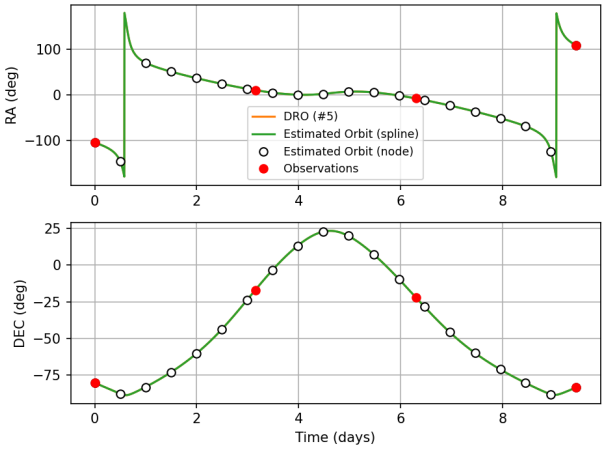

(b) Case 2 (DRO)

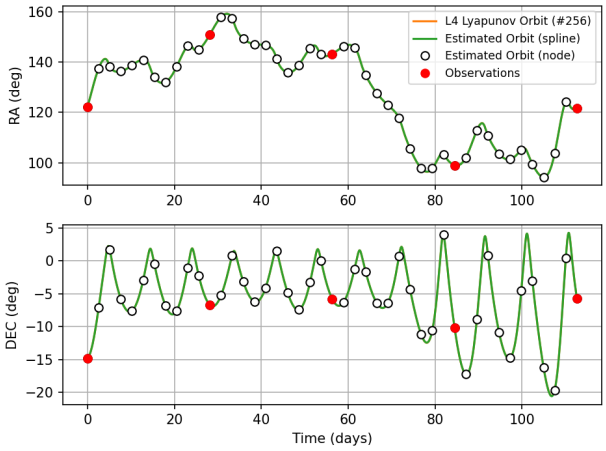

(c) Case 3 (L4 Long Period)

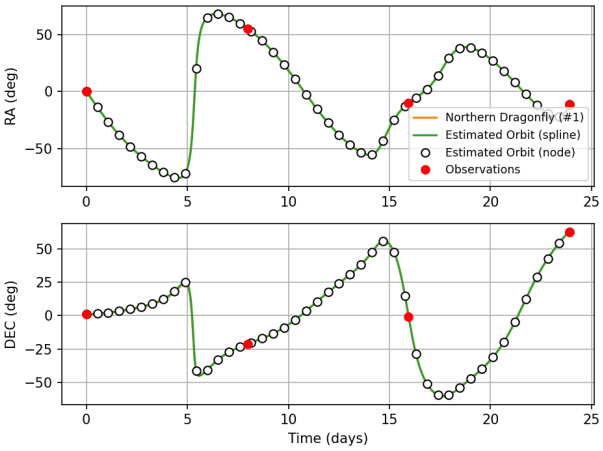

(d) Case 4 (Northern Dragonfly)

Fig. 5: Reconstructed observations using collocation IOD algorithm.

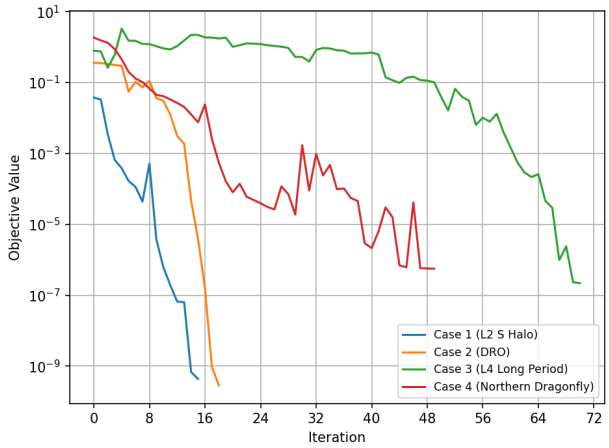

Fig. 6: IOD objective value versus NLP iteration for each observing case.

4.2 Transcription to Nonlinear Programming Problem

The periodic IOD problem can be transcribed to a NLP problem following a similar process as the preceding sections. The normalized time domain is divided into N segments

$$\tau_k = \tau_1 < \tau_2 < \cdots < \tau_N \tag{29}$$

where $\tau_1 = -1$ and $\tau_N = 1$. Following the transcription approach in Eq. (11), the defect constraints are written as

$$\boldsymbol{g}_k(\boldsymbol{x}_k, \boldsymbol{x}_{k+1}, \tau_k, \tau_{k+1}) = \boldsymbol{0}, \quad k = 1, \ldots, N-1 \tag{30}$$

The states and unknown period are then concatenated into an augmented parameter vector in the following NLP problem

$$\left(P^{N,1}\right) \begin{cases} \text{minimize} & J(\boldsymbol{X}, T) \\ \text{subject to} & \boldsymbol{g}(\boldsymbol{X}, T) = \boldsymbol{0} \\ & \boldsymbol{X}_L \leq \boldsymbol{X} \leq \boldsymbol{X}_U \\ & T_L \leq T \leq T_U \end{cases} \tag{31}$$

where T_L and T_U are the lower and upper bounds, respectively, on the unknown period T. These bounds can be set based on the predicted orbit family period range, or set arbitrarily large to explore a greater number of potential orbits. The periodicity requirement is enforced by an additional NLP constraint, giving a total of nN constraints and $nN+1$ unknowns.

4.3 Gradient and Jacobian Structure

In order to solve the NLP problem in Eq. (31), common solvers will require gradient and constraint Jacobian information. These expressions are similar to those developed in preceding sections, with the exception of an additional constraint and unknown due to the periodicity constraint. Equations (20) and (21) give the objective gradient with respect to the state at nodes k and $k+1$. A derivative is also required in order to evaluate the sensitivity with respect to the unknown period, T. Applying the chain rule to Eq. (10) gives

$$\frac{\partial J}{\partial T} = -2(\boldsymbol{y}_i - \boldsymbol{h}(\boldsymbol{x}_i, t_i))^{\mathrm{T}} R_i^{-1} \left(\frac{\partial \boldsymbol{h}_i}{\partial \boldsymbol{x}_i}\right) \left(\frac{\partial \boldsymbol{x}_i}{\partial \tau_i}\right) \frac{\partial \tau_i}{\partial T} \tag{32}$$

The second term $(\partial \boldsymbol{x}_i)/(\partial \tau_i)$ can be found from taking a derivative of Eq. (16) with respect to T, giving

$$\left(\frac{\partial \boldsymbol{x}_i}{\partial T}\right) = \boldsymbol{c}_1(\boldsymbol{x}_k, \boldsymbol{x}_{k+1}) + 2\boldsymbol{c}_2(\boldsymbol{x}_k, \boldsymbol{x}_{k+1})\Delta_i + 3\boldsymbol{c}_2(\boldsymbol{x}_k, \boldsymbol{x}_{k+1})\Delta_i^2 \ldots \tag{33}$$

where $\Delta_i = \tau_i - \tau_k$ in normalized time coordinates. These derivatives are given in the Appendix as a function of the transcription scheme. The last derivative in Eq. (32) can be found by inverting Eq. (26) for τ_i and taking a derivative with respect to T

$$\frac{\partial \tau_i}{\partial T} = -\frac{1}{T} + \frac{T - 2t_i}{T^2} \tag{34}$$

where we note that the measurement times t_i appear in non-normalized time coordinates. Equation (34) is ill-defined for $T \to 0$. Fortunately, this scenario of minimal concern for practical orbits, which generally must have a non-zero period.

It also helpful to outline the objective gradient and constraint Jacobian structures. For convenience, define the augmented state vector $\boldsymbol{Z} \in \mathbb{R}^{nN+1}$ as

$$\boldsymbol{Z}^{\mathrm{T}} = [\boldsymbol{X}^{\mathrm{T}}, T] \tag{35}$$

It can be shown that the non-zero entries of the objective gradient take the following structure

$$\left(\frac{\partial J}{\partial \boldsymbol{Z}}\right)^{\mathrm{T}} \sim \left[\begin{array}{ccccccccc|c} \boldsymbol{1}_n^{\mathrm{T}} & \boldsymbol{1}_n^{\mathrm{T}} & \boldsymbol{0}_n^{\mathrm{T}} & \cdots & \boldsymbol{0}_n^{\mathrm{T}} & \boldsymbol{1}_n^{\mathrm{T}} & \boldsymbol{1}_n^{\mathrm{T}} & \cdots & 1 \end{array}\right]^{\mathrm{T}} \in \mathbb{R}^{Nn+1} \tag{36}$$

Similarly, the constraint Jacobian has the structure

$$\left(\frac{\partial \boldsymbol{g}}{\partial \boldsymbol{Z}}\right) \sim \left[\begin{array}{ccccc|c} \boldsymbol{1}_{n\times n} & \boldsymbol{1}_{n\times n} & \boldsymbol{0}_{n\times n} & \cdots & \boldsymbol{0}_{n\times n} & \boldsymbol{1}_n \\ \boldsymbol{0}_{n\times n} & \boldsymbol{1}_{n\times n} & \boldsymbol{1}_{n\times n} & \cdots & \boldsymbol{0}_{n\times n} & \boldsymbol{1}_n \\ \vdots & \vdots & \ddots & \ddots & \vdots & \vdots \\ \boldsymbol{0}_{n\times n} & \boldsymbol{0}_{n\times n} & \cdots & \boldsymbol{1}_{n\times n} & \boldsymbol{1}_{n\times n} & \boldsymbol{1}_n \\ \hline \boldsymbol{I}_{n\times n} & \boldsymbol{0}_{n\times n} & \cdots & \boldsymbol{0}_{n\times n} & \boldsymbol{I}_{n\times n} & \boldsymbol{0}_n \end{array}\right] \in \mathbb{R}^{Nn\times Nn+1} \tag{37}$$

Target Orbit	Initial Guess	True Period (TU)	Estimated Period (TU)	Residual, $\|\boldsymbol{x}_1 - \boldsymbol{x}_N\|$
L2 S Halo	L2	3.4155	3.4157	2.8575E-4
Northern Dragonfly	L2	2.7551	2.7585	8.8564E-5

Table 2: Summary of periodic IOD results (L1 N Halo observer).

Note that the preceding equations are not strict equalities and serve only to show non-zero entries. The defect constraint equations depend on the period T through the affine time transformation in Eq. (26). Given the objective gradient and constraint Jacobian, the NLP problem in Eq. (31) can be solved to fit a periodic orbit to observed measurements.

4.4 Case Studies and Discussion

The periodic IOD algorithm is validated for a subset of cislunar observing cases in Table 2. In each observing scenario, a sequence of three measurements is used to reconstruct both the target orbit and an estimate of its period. Figure 7 shows these 3-D reconstructed orbits. Although the measurement interval covers less than half of each orbit, the resulting trajectory extends for full period to account for the periodicity constraint. In numerical experimentation, it was noted that the NLP solver can sometimes become "trapped" at Lagrange points, as these points trivially satisfy the periodicity constraint by remaining stationary. A simple resolution to this issue is introduce a small, random perturbation to the initial guess to allow the solver to explore wider regions of the solution space.

Figure 8 shows the observer-relative RA/DEC angles for the true and reconstructed orbits, as well as the measurement epochs. Following the final measurement, the remaining trajectory is stretched (or compressed) in time by the affine transformation in Eq. (26) as the estimated period changes. Accuracy of the results is further supported by Figure 9, which shows the estimated period in days for each NLP iteration. In both cases, the final estimated period converges to within 0.2% of the true period, even without a close initial guess.

Estimating the period of an object in non-Keplerian IOD has benefits from an operations perspective. Knowledge of an orbit period provides valuable information on sensor revisit rates and allows operators to predict when the object will be next observable. However, the method does present a few drawbacks. First, solution requires a greater number of collocation nodes, which increases computational requirements. Second, the solver may not always reliably converge to the correct solution, even while satisfying the periodicity constraint in the NLP algorithm. Additionally, orbits with longer periods (such as L4 or L5 orbits) have difficulty converging, although using AR methodologies to generate a more accurate initial guess may help overcome these challenges. Finally, it is important to note that periodic orbits are derived in the CR3BP system but may not exist in a true ephemeris model. However, the idealized CR3BP dynamics are often used to develop periodic trajectories for reference tracking and mission analysis.

This work develops a plausible concept for periodic IOD using direct methods, demonstrating its utility in cislunar SSA. Results of the IOD algorithm show promise for reconstructing periodic orbits from optical angles-only measurements. The findings of this work are expected to provide a highly robust and efficient algorithm for orbit determination in non-Keplerian systems. Potential future improvements to the methodology include adaptive mesh refinement techniques [6] or higher-order transcription methods [2].

5. CONCLUSIONS

This work outlines a novel non-Keplerian IOD algorithm leveraging direct collocation methods. The approach has a wide region of convergence and decreased sensitivity to initial guess errors. Results show the algorithm can reliably converge starting from initialization at one of the Lagrange points of the Earth-Moon system. Further, the method works well with sparse grids and large observing gaps, enabling rapid orbit determination with limited measurement information. A further modification of the algorithm is made for periodic orbit determination, which is shown to successfully reconstruct natural repeating orbits in the CR3BP system. The method provides a highly flexible, robust approach to cislunar SSA observing requiring minimal human supervision. Implications for this work include automated catalog maintenance and orbit determination for newly-detected objects in cislunar space. Future work includes validation of the approach on experimentally-obtained optical measurements. The method could also be extended to account for admissible regions or maneuvering targets. Finally, while optical angles-only measurements are the focus of this paper, the algorithm could be extended to include RF measurements instead.

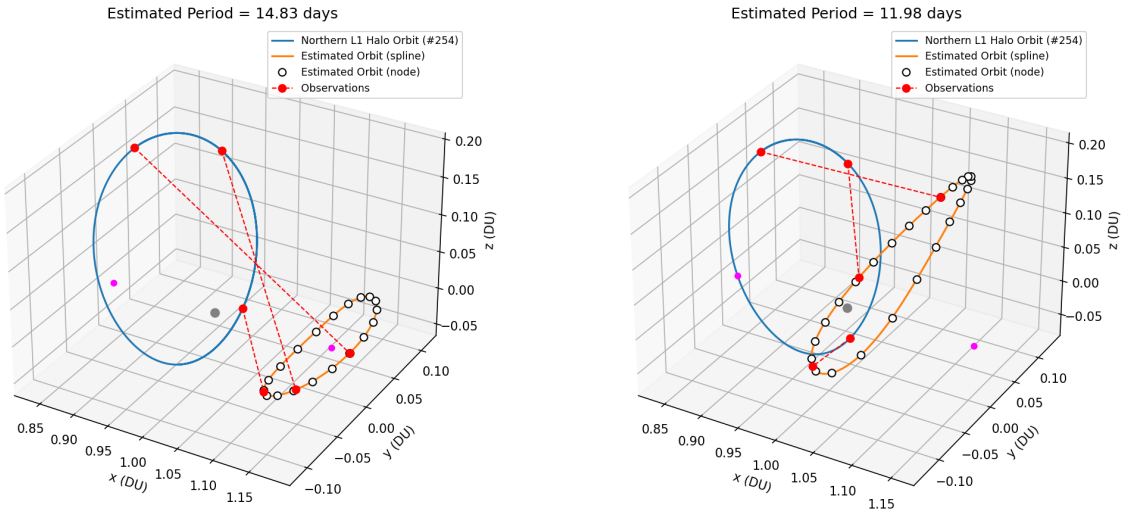

(a) L2 S Halo

(b) Northern Dragonfly

Fig. 7: Angles-only reconstructed orbits using periodic IOD algorithm.

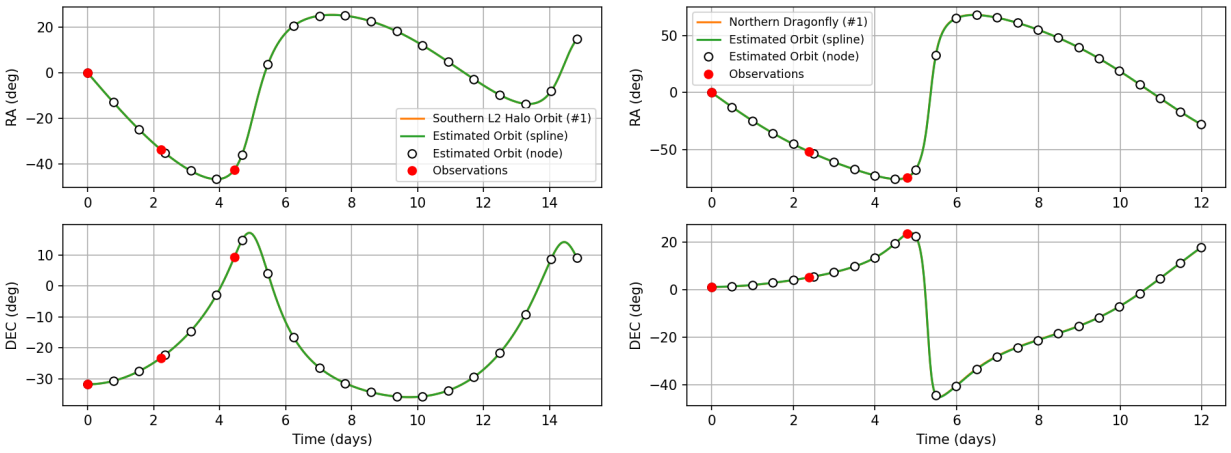

(a) L2 S Halo

(b) Northern Dragonfly

Fig. 8: Reconstructed observations using periodic IOD algorithm.

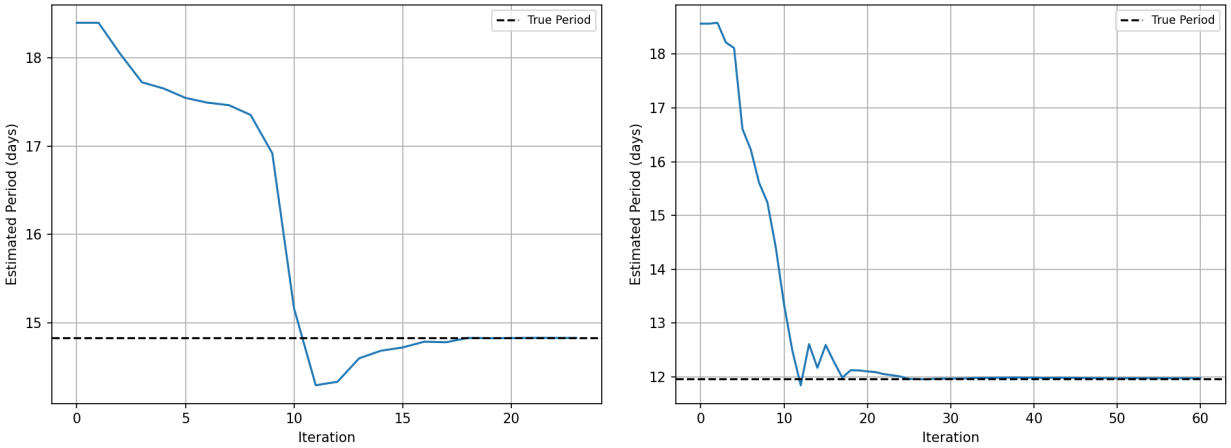

(a) L2 S Halo

(b) Northern Dragonfly

Fig. 9: Estimated period versus NLP iteration using periodic IOD algorithm.

ACKNOWLEDGEMENTS

Support for this research was provided through an AFRL Cooperative Agreement (award No. FA9453-22-2-0050) at the University of Colorado Boulder. The authors gratefully acknowledge technical discussion and advice from Jill Bruer and David Monet at AFRL/RVSW.

6. REFERENCES

[1] Roberto Barrio, Manuel Palacios, and Antonio Elipe. Chebyshev collocation methods for fast orbit determination. *Applied Mathematics and Computation*, 99(2-3):195–207, 1999.

[2] John T Betts. *Practical methods for optimal control and estimation using nonlinear programming*. SIAM, 2010.

[3] Lorenz T Biegler and Victor M Zavala. Large-scale nonlinear programming using ipopt: An integrating framework for enterprise-wide dynamic optimization. *Computers & Chemical Engineering*, 33(3):575–582, 2009.

[4] Ben K Bradley, Brandon A Jones, Gregory Beylkin, Kristian Sandberg, and Penina Axelrad. Bandlimited implicit runge–kutta integration for astrodynamics. *Celestial Mechanics and Dynamical Astronomy*, 119:143–168, 2014.

[5] C Channing Chow, Charles J Wetterer, Jason Baldwin, Micah Dilley, Keric Hill, Paul Billings, and James Frith. Cislunar orbit determination behavior: Processing observations of periodic orbits with gaussian mixture model estimation filters. *The Journal of the Astronautical Sciences*, 69(5):1477–1492, 2022.

[6] Christopher L Darby, William W Hager, and Anil V Rao. An hp-adaptive pseudospectral method for solving optimal control problems. *Optimal Control Applications and Methods*, 32(4):476–502, 2011.

[7] Pedro Escobal. Methods of orbit determination. *Methods of orbit determination*, 1970.

[8] C Frueh, K Howell, K DeMars, S Bhadauria, and M Gupta. Cislunar space traffic management: Surveillance through earth-moon resonance orbits. In *8th European Conference on Space Debris*, volume 8, 2021.

[9] Kohei Fujimoto and Daniel J Scheeres. Correlation of optical observations of earth-orbiting objects and initial orbit determination. *Journal of guidance, control, and dynamics*, 35(1):208–221, 2012.

[10] Kohei Fujimoto, Daniel J Scheeres, Johannes Herzog, and Thomas Schildknecht. Association of optical tracklets from a geosynchronous belt survey via the direct bayesian admissible region approach. *Advances in space research*, 53(2):295–308, 2014.

[11] Divya Garg, Michael A Patterson, Camila Francolin, Christopher L Darby, Geoffrey T Huntington, William W Hager, and Anil V Rao. Direct trajectory optimization and costate estimation of finite-horizon and infinite-horizon optimal control problems using a radau pseudospectral method. *Computational Optimization and Applications*, 49:335–358, 2011.

[12] Philip E Gill, Walter Murray, and Michael A Saunders. Snopt: An sqp algorithm for large-scale constrained optimization. *SIAM review*, 47(1):99–131, 2005.

[13] RH Gooding. *A new procedure for orbit determination based on three lines of sight (angles only)*. Defence Research Agency Farnborough, UK, 1993.
[14] Zach Hall, David Schwab, Roshan Eapen, and Puneet Singla. Reachability-based approach for search and detection of maneuvering cislunar objects. In *AIAA SCITECH 2022 Forum*, page 0853, 2022.
[15] MJ Holzinger, CC Chow, and P Garretson. *A primer on cislunar space*. Air Force Research Laboratory, 2021.
[16] Brandon Jones. Orbit propagation using gauss-legendre collocation. In *AIAA/AAS Astrodynamics Specialist Conference*, page 4967, 2012.
[17] Matthew Kelly. An introduction to trajectory optimization: How to do your own direct collocation. *SIAM Review*, 59(4):849–904, 2017.
[18] Greg Martin, Charles J Wetterer, Jenna Lau, Jeremy Case, Nathan Toner, C Channing Chow, and Phan Dao. Cislunar periodic orbit family classification from astrometric and photometric observations using machine learning. In *2020 Advanced Maui Optical and Space Surveillance Technologies Conference (AMOS)*, 2020.
[19] Yingjing Qian, Chaoyong Li, Wuxing Jing, Inseok Hwang, and Jian Wei. Sun–earth–moon autonomous orbit determination for quasi-periodic orbit about the translunar libration point and its observability analysis. *Aerospace Science and Technology*, 28(1):289–296, 2013.
[20] Anil V Rao. A survey of numerical methods for optimal control. *Advances in the astronautical Sciences*, 135(1):497–528, 2009.
[21] Sean Tang and Bruce A Conway. Optimization of low-thrust interplanetary trajectories using collocation and nonlinear programming. *Journal of Guidance, Control, and Dynamics*, 18(3):599–604, 1995.
[22] Francesco Topputo, Chen Zhang, et al. Survey of direct transcription for low-thrust space trajectory optimization with applications. In *Abstract and Applied Analysis*, volume 2014. Hindawi, 2014.
[23] Samuel Wishnek, Marcus J Holzinger, and Patrick Handley. Robust cislunar initial orbit determination. In *AMOS Conf. Proc*, 2021.
[24] Johnny L Worthy III and Marcus J Holzinger. Incorporating uncertainty in admissible regions for uncorrelated detections. *Journal of Guidance, Control, and Dynamics*, 38(9):1673–1689, 2015.
[25] Johnny L Worthy III, Marcus J Holzinger, and Daniel J Scheeres. An optimization approach for observation association with systemic uncertainty applied to electro-optical systems. *Advances in Space Research*, 61(11):2709–2724, 2018.
[26] David Zuehlke, Taylor Yow, Daniel Posada, Joseph Nicolich, Christopher W Hays, Aryslan Malik, and Troy Henderson. Initial orbit determination for the cr3bp using particle swarm optimization. *arXiv preprint arXiv:2207.13175*, 2022.

A. APPENDIX: DERIVATIVE QUANTITIES

This appendix outlines the necessary derivative quantities for evaluating the NLP objective gradient and constraint Jacobian. Expressions are organized with respect to each transcription method for clarity.

A.1 Trapezoidal Collocation

The following derivatives are necessary to compute the interpolation gradient with respect to nodes k and $k+1$ in Eq. (20) and (21) using trapezoidal quadrature.

The trapezoidal interpolation scheme is repeated from Eq. (12) as follows

$$\boldsymbol{x}_i = \boldsymbol{x}_k + \boldsymbol{f}_k \Delta_i + \frac{1}{2}\frac{\Delta_i^2}{h_k}(\boldsymbol{f}_{k+1} - \boldsymbol{f}_k) \tag{38}$$

giving the following derivatives at nodes k and $k+1$

$$\left(\frac{\partial \boldsymbol{x}_i}{\partial \boldsymbol{x}_k}\right) = \boldsymbol{I}_{n\times n} + \left(\frac{\partial \boldsymbol{f}_k}{\partial \boldsymbol{x}_k}\right)\left(\Delta_i - \frac{1}{2}\frac{\Delta_i^2}{h_k}\right) \tag{39}$$

$$\left(\frac{\partial \boldsymbol{x}_i}{\partial \boldsymbol{x}_{k+1}}\right) = \left(\frac{\partial \boldsymbol{f}_{k+1}}{\partial \boldsymbol{x}_{k+1}}\right)\frac{1}{2}\frac{\Delta_i^2}{h_k} \tag{40}$$

For the periodic IOD derivative in Eq. (33), the following derivative is also required

$$\left(\frac{\partial \boldsymbol{x}_i}{\partial T}\right) = \boldsymbol{f}_k + \frac{\Delta_i}{h_k}(\boldsymbol{f}_{k+1} - \boldsymbol{f}_k) \tag{41}$$

The defect constraints for trapezoidal quadrature are also repeated from Eq. (12) here

$$\boldsymbol{g}_k = \boldsymbol{x}_{k+1} - \boldsymbol{x}_k - \frac{1}{2}h_k(\boldsymbol{f}_{k+1} + \boldsymbol{f}_k) = \boldsymbol{0} \tag{42}$$

giving the following Jacobian at nodes k and $k+1$

$$\left(\frac{\partial \boldsymbol{g}_k}{\partial \boldsymbol{x}_k}\right) = -\boldsymbol{I}_{n\times n} - \frac{1}{2}h_k\left(\frac{\partial \boldsymbol{f}_k}{\partial \boldsymbol{x}_k}\right) \tag{43}$$

$$\left(\frac{\partial \boldsymbol{g}_k}{\partial \boldsymbol{x}_{k+1}}\right) = \boldsymbol{I}_{n\times n} - \frac{1}{2}h_k\left(\frac{\partial \boldsymbol{f}_{k+1}}{\partial \boldsymbol{x}_{k+1}}\right) \tag{44}$$

These expressions complete the necessary derivative quantities using trapezoidal quadrature.

A.2 Hermite-Simpson Collocation

The trapezoidal interpolation scheme is repeated from Eq. (18) as follows

$$\boldsymbol{x}_i = \boldsymbol{x}_k + \boldsymbol{f}_k\Delta_i + \frac{1}{2h_k}(-3\boldsymbol{f}_k + 4\boldsymbol{f}_{k+\frac{1}{2}} - \boldsymbol{f}_{k+1})\Delta_i^2 + \frac{1}{3h_k^2}(2\boldsymbol{f}_k - 4\boldsymbol{f}_{k+\frac{1}{2}} + 2\boldsymbol{f}_{k+1})\Delta_i^3 \tag{45}$$

giving the following interpolation gradient with respect to nodes k and $k+1$ in Eq. (20) and (21)

$$\left(\frac{\partial \boldsymbol{x}_i}{\partial \boldsymbol{x}_k}\right) = \boldsymbol{I}_{n\times n} + \left(\frac{\partial \boldsymbol{f}_k}{\partial \boldsymbol{x}_k}\right)\left(\Delta_i - \frac{3}{2}\frac{\Delta_i^2}{h_k} + \frac{2}{3}\frac{\Delta_i^3}{h_k^2}\right) + \left(\frac{\partial \boldsymbol{f}_{k+\frac{1}{2}}}{\partial \boldsymbol{x}_k}\right)\left(2\frac{\Delta_i^2}{h_k} - \frac{4}{3}\frac{\Delta_i^3}{h_k^2}\right) \tag{46}$$

$$\left(\frac{\partial \boldsymbol{x}_i}{\partial \boldsymbol{x}_{k+1}}\right) = \left(\frac{\partial \boldsymbol{f}_{k+1}}{\partial \boldsymbol{x}_{k+1}}\right)\left(-\frac{1}{2}\frac{\Delta_i^2}{h_k} + \frac{2}{3}\frac{\Delta_i^3}{h_k^2}\right) + \left(\frac{\partial \boldsymbol{f}_{k+\frac{1}{2}}}{\partial \boldsymbol{x}_{k+1}}\right)\left(2\frac{\Delta_i^2}{h_k} - \frac{4}{3}\frac{\Delta_i^3}{h_k^2}\right) \tag{47}$$

where from Eq. (14) it can be shown that

$$\left(\frac{\partial \boldsymbol{f}_{k+\frac{1}{2}}}{\partial \boldsymbol{x}_k}\right) = \left(\frac{\partial \boldsymbol{f}_{k+\frac{1}{2}}}{\partial \boldsymbol{x}_{k+\frac{1}{2}}}\right)\left[\frac{1}{2}\boldsymbol{I}_{n\times n} + \frac{h_k}{8}\left(\frac{\partial \boldsymbol{f}_k}{\partial \boldsymbol{x}_k}\right)\right] \tag{48}$$

$$\left(\frac{\partial \boldsymbol{f}_{k+\frac{1}{2}}}{\partial \boldsymbol{x}_{k+1}}\right) = \left(\frac{\partial \boldsymbol{f}_{k+\frac{1}{2}}}{\partial \boldsymbol{x}_{k+\frac{1}{2}}}\right)\left[\frac{1}{2}\boldsymbol{I}_{n\times n} - \frac{h_k}{8}\left(\frac{\partial \boldsymbol{f}_{k+1}}{\partial \boldsymbol{x}_{k+1}}\right)\right] \tag{49}$$

which gives expressions evaluated at the midpoint of the segment. For the periodic IOD derivative in Eq. (33), the following derivative is also required

$$\left(\frac{\partial \boldsymbol{x}_i}{\partial T}\right) = \boldsymbol{f}_k + \frac{1}{h_k}(-3\boldsymbol{f}_k + 4\boldsymbol{f}_{k+\frac{1}{2}} - \boldsymbol{f}_{k+1})\Delta_i + \frac{1}{h_k^2}(2\boldsymbol{f}_k - 4\boldsymbol{f}_{k+\frac{1}{2}} + 2\boldsymbol{f}_{k+1})\Delta_i^2 \tag{50}$$

The defect constraints for Hermite-Simpson quadrature are also repeated from Eq. (13) here

$$\boldsymbol{g}_k = \boldsymbol{x}_{k+1} - \boldsymbol{x}_k - \frac{1}{6}h_k(\boldsymbol{f}_k + 4\boldsymbol{f}_{k+\frac{1}{2}} + \boldsymbol{f}_{k+1}) = \boldsymbol{0} \tag{51}$$

giving the following Jacobian at nodes k and $k+1$

$$\left(\frac{\partial \boldsymbol{g}_k}{\partial \boldsymbol{x}_k}\right) = -\boldsymbol{I}_{n\times n} - \frac{1}{6}h_k\left[\left(\frac{\partial \boldsymbol{f}_k}{\partial \boldsymbol{x}_k}\right) + 4\left(\frac{\partial \boldsymbol{f}_{k+\frac{1}{2}}}{\partial \boldsymbol{x}_k}\right)\right] \tag{52}$$

$$\left(\frac{\partial \boldsymbol{g}_k}{\partial \boldsymbol{x}_{k+1}}\right) = \boldsymbol{I}_{n\times n} - \frac{1}{6}h_k\left[4\left(\frac{\partial \boldsymbol{f}_{k+\frac{1}{2}}}{\partial \boldsymbol{x}_{k+1}}\right) + \left(\frac{\partial \boldsymbol{f}_{k+1}}{\partial \boldsymbol{x}_{k+1}}\right)\right] \tag{53}$$

These expressions complete the necessary derivative quantities using Hermite-Simpson quadrature.